Nanoscale

ROYAL SOCIETY OF CHEMISTRY

PAPER

View Article Online
View Journal | View Issue

Cite this: *Nanoscale*, 2025, **17**, 2554

Ultrasensitive non-enzymatic electrochemical detection of paraoxon-ethyl in fruit samples using 2D $Ti_3C_2T_x$/MWCNT-OH†

Asmi Aris, [a,b] Wulan Tri Wahyuni, [c,d] Budi Riza Putra, [e] Angga Hermawan, [f] Ferry Anggoro Ardy Nugroho, [g,h] Zhi Wei Seh *[i] and Munawar Khalil *[a,b,h]

Received 2nd October 2024,
Accepted 30th December 2024

DOI: 10.1039/d4nr04060k

rsc.li/nanoscale

This study reports on the development of a highly sensitive non-enzymatic electrochemical sensor based on a two-dimensional $Ti_3C_2T_x$/MWCNT-OH nanocomposite for the detection of paraoxon-based pesticide. The synergistic effect between the $Ti_3C_2T_x$ nanosheet and the functionalized multi-walled carbon nanotubes enhanced the sensor's conductivity and catalytic activity. The nanocomposite demonstrates superior electrochemical and electroanalytical performance compared to the pristine $Ti_3C_2T_x$ and MWCNT-OH in detecting paraoxon-ethyl in fruit samples (green and red grapes), with a linear response range from 0.1 to 100 μM, a low limit of detection (LOD) of 10 nM, limit of quantitation (LOQ) of 70 nM, and sensitivity of 0.957 μA μM^{-1} cm^{-2} at pH 8. Furthermore, the sensors maintain excellent selectivity and effectiveness in detecting paraoxon-ethyl even in the presence of various interferents, including diazinon, carbaryl, Fe^{2+}, NO_2^-, NO_3^-, ascorbic acid, and glucose. The facile fabrication and enhanced sensing capabilities of the $Ti_3C_2T_x$/MWCNT-OH nanocomposite position it as a reliable, cost-effective, and sustainable alternative to conventional detection systems for monitoring pesticide residues in agricultural products.

Introduction

The development of advanced electrochemical sensors for detecting pesticides is crucial in addressing the widespread use of these toxic compounds in agriculture.[1–3] The remnants of pesticides present on crops and soil after application often pose significant health risks to humans and can lead to environmental contamination. Currently, organophosphates such as paraoxon-ethyl are among the most used pesticides in agriculture.[4–6] However, the presence of such pesticides in food and water sources can lead to serious human health issues. Exposure to paraoxon-ethyl at certain doses can provoke anxiolytic behavior, impact the nervous system *via* specific toxic mechanisms, inhibit the enzyme acetylcholinesterase, and ultimately lead to neurological damage, severe physiological effects, and cardiovascular diseases.[7–9] Therefore, accurate and efficient monitoring of these substances is crucial for ensuring food safety, environmental protection, and public health.

Over the years, several techniques for detecting paraoxon-ethyl have been developed, including colorimetry, fluorometry, enzyme-based biosensors, chromatography, and spectroscopy.[10–15] However, most of these detection methods demand extensive sample preparation, making them unsuitable for rapid testing, and often requiring skilled operators. Besides, some of these detection techniques suffer from a lack of specificity and sensitivity in detecting low concentrations and are prone to interference from various contaminants in real samples.[16,17] Recently, electrochemical detection methods have gained popularity due to their rapid response times, high sensitivity, and the potential for miniaturization and integration into portable devices.[18–21] These detection techniques

[a]*Department of Chemistry, Faculty of Mathematics and Natural Sciences, Universitas Indonesia, 16424 Depok, West Java, Indonesia. E-mail: mkhalil@sci.ui.ac.id*
[b]*Low Dimension Materials Lab, Department of Chemistry, Faculty of Mathematics and Natural Sciences, Universitas Indonesia, 16424 Depok, West Java, Indonesia*
[c]*Department of Chemistry, Faculty of Mathematics and Natural Sciences, IPB University, 16680 Bogor, Indonesia*
[d]*Tropical Biopharma Research Center, IPB University, 16680 Bogor, Indonesia*
[e]*Research Center for Metallurgy, National Research and Innovation Agency (BRIN), South Tangerang, Banten 15315, Indonesia*
[f]*Research Center for Nanotechnology System, National Research and Innovation Agency (BRIN), South Tangerang, Banten 15314, Indonesia*
[g]*Department of Physics, Faculty of Mathematics and Natural Sciences, Universitas Indonesia, 16424 Depok, West Java, Indonesia*
[h]*Institute for Advanced Sustainable Materials Research and Technologies (INA-SMART), Faculty of Mathematics and Natural Sciences, Universitas Indonesia, 16424 Depok, West Java, Indonesia*
[i]*Institute of Materials Research and Engineering (IMRE), Agency for Science, Technology and Research (A*STAR), 2 Fusionopolis Way, Innovis #08-03, Singapore 138634, Republic of Singapore. E-mail: sehzw@imre.a-star.edu.sg*
† Electronic supplementary information (ESI) available. See DOI: https://doi.org/10.1039/d4nr04060k

offer real-time monitoring and on-site analysis, critical for immediate decision-making and intervention in agricultural settings.[22,23] The capability of electrochemical sensors to function effectively in complex matrices, like soil or food samples, without extensive sample preparation provides a significant practical advantages. This is particularly important given the rising regulatory demands for environmental monitoring and the need for more sustainable agricultural practices that minimize pesticide use and its associated risks.

During the past several years, the utilization of two-dimensional (2D) materials in the fabrication of electrochemical sensors for pesticide residues has showcased significant potential due to their unique properties.[24–26] Among these 2D materials, MXenes, composed of transition metal carbides, nitrides, and carbonitrides, have garnered considerable attention for its diverse surface functionalities and suitable band gap, making it ideal for various applications, including electrochemical sensors.[27] In particular, the utilization of $Ti_3C_2T_x$ MXene as an active material in sensing devices has received tremendous attention due to its excellent metallic conductivity, high hydrophilicity, fast electron transfer rates, and large surface area for interaction with target molecules.[28–31] For example, Yu and co-workers have successfully used cobalt-doped Ti_3C_2 MXene nanosheets for the detection of pesticide residues in pakchoi.[32] The developed homogeneous electrochemical (HEC) sensors tackled common sensor issues like high background signal and low signal-to-noise ratio. The sensor exhibited peroxidase-like properties which are responsible for enhancing organophosphate pesticide detection by catalyzing the hydrolysis of acetylthiocholine. In another study, Zhao *et al.* reported that the integration of MXene and Au–Pd bimetallic nanoparticles on acetylcholinesterase enzyme enhanced the detection ability of the as-prepared biosensor towards paraoxon.[33] The biosensor demonstrated a detection range for paraoxon from 0.1 to 1000 μg L^{-1} and effectively detected the pesticide in pear and cucumber samples, showcasing the potential of 2D nanomaterials in biosensing. Furthermore, an electrochemical sensor based on $Ti_3C_2T_x$-derived sodium titanate nanoribbons (MNR) was reported to be effective for detecting pesticides in various vegetable extracts.[34] This sensor showed a low detection limit of 0.22 nM and a broad detection range of up to 174.03 nM for ethyl paraoxon, demonstrating high sensitivity and potential for real sample applications. However, 2D $Ti_3C_2T_x$ suffers from natural re-stacking that prevents efficient electron transfer and limits the accessibility of active sites. To overcome this limitation, the incorporation of mechanically robust conductive binder has been explored to prevent the restacking of 2D $Ti_3C_2T_x$ and improve their performance as active materials for the electrochemical sensor.

In recent development, multi-walled carbon nanotubes (MWCNT) have been found to complement the utilization of $Ti_3C_2T_x$ by enhancing its overall conductivity and mechanical strength, which are essential for durable, reusable sensors.[35–37] It is reported that the tubular structure of MWCNT prevents stacking of 2D $Ti_3C_2T_x$ and provides a robust framework for electron pathways, reducing the overall resistance of the nanocomposite.[38,39] Furthermore, MWCNT-OH demonstrates improved stability due to the presence of surface functional groups that enhance hydrogen bonding, converting its surface from hydrophobic to hydrophilic. This results in higher hydrophilicity and polarity compared to MWCNT. Therefore, the present study aims to develop an electrochemical sensor based on a $Ti_3C_2T_x$/MWCNT-OH nanocomposite to enhance the detection of paraoxon-ethyl pesticide in fruit samples. Here, $Ti_3C_2T_x$ was prepared *via* selective etching method, while MWCNT was acid-functionalized to introduce hydroxyl groups responsible for facilitating its incorporation with $Ti_3C_2T_x$. The performance of the nanocomposite in detecting paraoxon-ethyl was evaluated and compared with its components by determining several electrochemical detection parameters, such as linearity, limit of detection (LOD), and limit of quantification (LOQ). Besides, the selectivity of sensor was also evaluated in the presence of several interfering species. The key goal is to design a sensor that fits smoothly into current monitoring infrastructures, providing a practical means for ongoing surveillance and compliance with pesticide safety standards. This initiative fulfills a crucial role in agricultural safety and enriches materials science by demonstrating the utility of new nanocomposites in sensitive detection applications.

Experimental methods

Materials

Titanium aluminium carbon (Ti_3AlC_2) MAX phase (325 mesh, purity ~98%) was purchased from Advanced Materials Development Expert Store, China. Hydrogen fluoride (HF, 48% weight in H_2O, purity 99.9%), hydrochloric acid (HCl, 37% weight in H_2O, purity 99.99%), and dimethyl sulfoxide (DMSO, purity 99.9%) from Sigma-Aldrich were used in the synthesis of $Ti_3C_2T_x$. Multi-walled carbon nanotubes (MWCNTs, length: 5–9 μm, purity >97%), hydrogen peroxide (H_2O_2, 30% weight in H_2O, purity 99.9%), and nitric acid (HNO_3, 65% weight in H_2O, purity 99.99%) from Sigma-Aldrich were utilized in the preparation of hydroxylated multi-walled carbon nanotubes (MWCNTs-OH). Sodium phosphate monobasic (NaH_2PO_4, purity 99%), sodium phosphate dibasic (Na_2HPO_4, purity 99.99%), and sodium hydroxide (NaOH, purity 99.5%) from Sigma-Aldrich were used to prepare the phosphate buffer solution at pH 8. Additionally, potassium chloride (KCl, purity 99.99%) was obtained from HiMedia. Diethyl 4-nitrophenyl phosphate or paraoxon-ethyl (POE, CAS: 311-45-5), potassium hexacyanoferrate(III) ($K_3[Fe(CN)_6]$, CAS: 13746-66-2), diazinon, carbaryl (CAS: 63-25-2), iron(II) sulfate heptahydrate ($FeSO_4$, purity 99.99%), sodium nitrite ($NaNO_2$, purity 99.99%), sodium nitrate ($NaNO_3$, purity: 99.99%), ascorbic acid ($C_6H_8O_6$, purity 99.99%), and glucose ($C_6H_{12}O_6$, purity 99.99%) from Sigma-Aldrich were utilized to prepare the analytes.

Synthesis of $Ti_3C_2T_x$

$Ti_3C_2T_x$ was prepared *via* the selective etching method, following our previous work.[29,30] Typical synthesis was carried out by

preparing an acidic mixture containing 10 mL of HF, 30 mL of deionized (DI) water, and 60 mL of 37 wt% HCl in a 250 mL polypropylene (PP) bottle. The solution was then stirred at 40 °C for 30 min. Subsequently, 10 g of Ti_3AlC_2 was incrementally added to the solution, followed by continuous stirring for 24 h at 40 °C. Post-stirring, the solution underwent ultrasonication for 30 min and was centrifuged at 3500 rpm for 5 minutes. The precipitate was then washed with DI water until the pH reached ~6. The precipitate was then collected and dried at 60 °C for 6 h. Next, 3 grams of the resulting powder was mixed with 50 mL of DMSO while stirred at 150 rpm for 24 h. The mixture was centrifuged at 3500 rpm for 5 min, and the precipitate was collected and washed with DI water several times. This precipitate was re-dispersed in 1500 mL of DI water, followed by sonication for 10 h. Finally, the mixture was vacuum filtered through mixed cellulose ester (MCE) filter paper and subsequently dried at 60 °C for 3 h to obtain the final $Ti_3C_2T_x$ powder.

Functionalization of MWCNT

The hydroxyl-functionalized multiwalled carbon nanotubes (MWCNT-OH) were prepared by using the following procedure. Initially, 0.3 g of MWCNTs was combined with 70 mL of 8 M HNO_3 in a reaction vessel. The mixture was stirred at 60 °C for 15 min, followed by 2 h of sonication. After that, the mixture was filtered, and the obtained precipitates were washed with DI water to remove any residual acid. Subsequently, the washed precipitates were then re-dispersed in 70 mL of 30% H_2O_2 solution. The mixture was stirred at 60 °C for 15 min and then ultrasonicated for 2 h. The mixture was then filtered and washed with DI water to remove any excess oxidizing agent. Finally, the washed precipitate was then collected and dried in an oven at 150 °C for 4 h to yield MWCNT-OH.

Preparation of $Ti_3C_2T_x$/MWCNT-OH nanocomposite

$Ti_3C_2T_x$/MWCNT-OH nanocomposite was fabricated by dispersing the as-prepared $Ti_3C_2T_x$ and MWCNT-OH in DI water at various weight ratios, *i.e.*, 10 : 0, 8 : 2, 6 : 4, 5 : 5, 4 : 6, 2 : 8, and 0 : 10 to achieve a final concentration of 1 mg mL^{-1}. The mixture was then stirred for 1 h followed by ultrasonication for 30 min. The dispersions were first stirred for 1 h to ensure homogeneous mixing, followed by ultrasonication for 30 min. These resulting mixtures were then denoted as the "active solutions" and were further used in the fabrication of sensing electrodes.

Fabrication of sensing electrode

The sensing electrodes were fabricated by drop-casting the as-prepared $Ti_3C_2T_x$, MWCNT-OH, and their composites at various weight ratios onto a glassy carbon electrode (GCE) surface. Specifically, 5 μL of the "active solution" containing the dispersed nanocomposite materials was drop-cast onto the GCE. The modified GCE electrodes were then heated in an oven at 85 °C for 6 min to dry and anchor the nanocomposite materials.

Characterizations

Various characterization techniques were employed to investigate the physicochemical properties of the prepared samples. X-ray diffraction (XRD) analysis was carried out using the Malvern Panalytical instrument (PANalytical B.V., Netherlands), operated at 40 kV and 30 mA with Cu-Kα radiation as the source. Raman spectroscopic analysis was performed using a Horiba LabRAM HR Evolution equipped with a 523 nm laser source. Fourier-transform infrared (FTIR) spectroscopy was performed using a Shimadzu IR Prestige-21 to identify the functional groups present in the prepared sample. Furthermore, the TECNAI G2 Spirit Twin transmission electron microscope (TEM) equipped with a LaB_6 filament and operating at 200 kV was used to provide detailed micrographic images of the samples. Additionally, surface morphology and elemental composition of the samples were also studied using Thermofisher Apreo 2 Field emission scanning electron microscope-energy dispersive X-ray spectroscopy (FESEM-EDS). Finally, detailed compositional and surface structural analyses were conducted using X-ray photoelectron spectroscopy (XPS) with the Kratos AXIS Supra+, and the data was processed using the specialized "ESCApe" software.

Electrochemical analysis

The electrochemical behaviors of the bare GCE and the prepared sensing electrodes were analyzed using 100 μM paraoxon-ethyl in 0.1 M phosphate buffer solution (PBS) at pH 7.0. Differential pulse voltammetry (DPV) was employed with a potential window ranging from −0.8 to −0.2 V *vs.* Ag/AgCl. The measurements were conducted at a scan rate of 50 mV s^{-1}, potential step of 5 mV, pulse amplitude of 50 mV, and pulse width of 0.05 s. Before further studying the electrochemical behavior and analytical performance, the composition optimization of various ratios between $Ti_3C_2T_x$ and MWCNT-OH was first conducted. Furthermore, the electrochemical behavior was evaluated based on different pH conditions, ranging from 5.0 to 10.0. Further evaluations were carried out to assess the electrode surface area, scan rate effect, diffusion coefficient values, and electrochemical impedance spectroscopy (EIS).

Sensing evaluation

The analytical performances of the sensor were further analyzed by determining several sensing parameters, including linearity, limit of detection (LOD), limit of quantification (LOQ), reproducibility, stability, sensitivity, and selectivity. Linearity for paraoxon-ethyl detection was evaluated across a concentration range of 1–100 μM in 0.1 M phosphate buffer at pH 8.0. To ensure accuracy and repeatability, all measurements were conducted in triplicate under identical conditions using the same DPV technique. A high coefficient of determination (R^2) close to 1 indicated optimal sensitivity for the paraoxon-ethyl detections. Additionally, sensitivity was also derived from the calibration curve by simply dividing the slope with surface area of the electrode. Here, the active surface area of GCE electrode was 0.31 cm^2. Finally, LOD and LOQ were estimated

using the signal-to-noise ratio (S/N) criteria where LOD (S/N ≈ 3) and LOQ (S/N ≈ 10).

To assess reproducibility, six identical sensing electrodes were prepared and used to measure 80 μM paraoxon-ethyl in 0.1 M phosphate buffer (pH 8.0) across three replicates. Meanwhile, the inter-day stability of the sensor was determined by continuously measuring 80 μM paraoxon-ethyl using a single electrode over five consecutive days in the same buffer solution. Both reproducibility and stability were quantified using the percentage relative standard deviation (%RSD) of paraoxon-ethyl measurements. The selectivity of the sensor was evaluated by measuring the response to 80 μM paraoxon-ethyl in the presence of various interfering substances, including diazinon, carbaryl, $NaNO_3$, $NaNO_2$, $FeSO_4$, ascorbic acid, and glucose, also at a concentration of 80 μM.

To evaluate the performance of the as-prepared sensor in detecting paraoxon-ethyl in real fruit samples, *i.e.*, green and red grapes, the DPV technique was employed. Typically, 2 mL of grape sample was spiked with paraoxon-ethyl standard solutions to obtain increasing concentrations of 1, 5, 10, 40, 60, and 80 μM. The spiked samples were subsequently diluted with 0.1 M PBS (pH 8.0) to reach a total volume of 10 mL. Here, the concentration of paraoxon-ethyl in the fruit samples was estimated from the *X*-intercept of the calibration curve established for each set of spiked and diluted standard solutions using the following equation:

$$X\text{-intercept} = -C_A \frac{V_0}{V_f} \quad (1)$$

where C_A represents the concentration of paraoxon-ethyl in the fruit samples, V_0 is the initial volume of the fruit sample, V_f is the final volume of the diluted fruit solution, and the *X*-intercept is obtained when the *y*-axis equals zero.

Results and discussion

Characterization of the sensing electrodes

Fig. 1a presents an X-ray diffractogram of the as-prepared samples and their nanocomposites. Based on the result, it is evident that Ti_3AlC_2 was successfully converted into $Ti_3C_2T_x$ using etching and exfoliation methods (see Fig. S1, ESI† for diffractogram of Ti_3AlC_2). The formation of $Ti_3C_2T_x$ was proven by a shift in the XRD diffraction peak corresponding to the (002) plane of Ti_3AlC_2 to a lower angle due to the etching of the Al layer and an increase in *d*-spacing parameters.[40] In addition, a significant decrease in the peak intensity of the (008) plane was also indicative of the removal of alumina and aluminum layers from Ti_3AlC_2.[40,41] The XRD analysis also revealed the characteristic peaks corresponding to the (002) and (001) planes of graphite, indicating the successful functionalization of the MWCNT.[42,43] Furthermore, the results demonstrate that a simple ultrasonic method was able to effectively integrate both $Ti_3C_2T_x$ and MWCNT-OH, as evidenced by the appearance of the characteristic peaks for both materials in the nanocomposite (Fig. 1a).

The observation from the X-ray diffraction analysis was further supported by Raman spectroscopy. Fig. 1b presents Raman spectra of $Ti_3C_2T_x$, MWCNT-OH, and their composite.

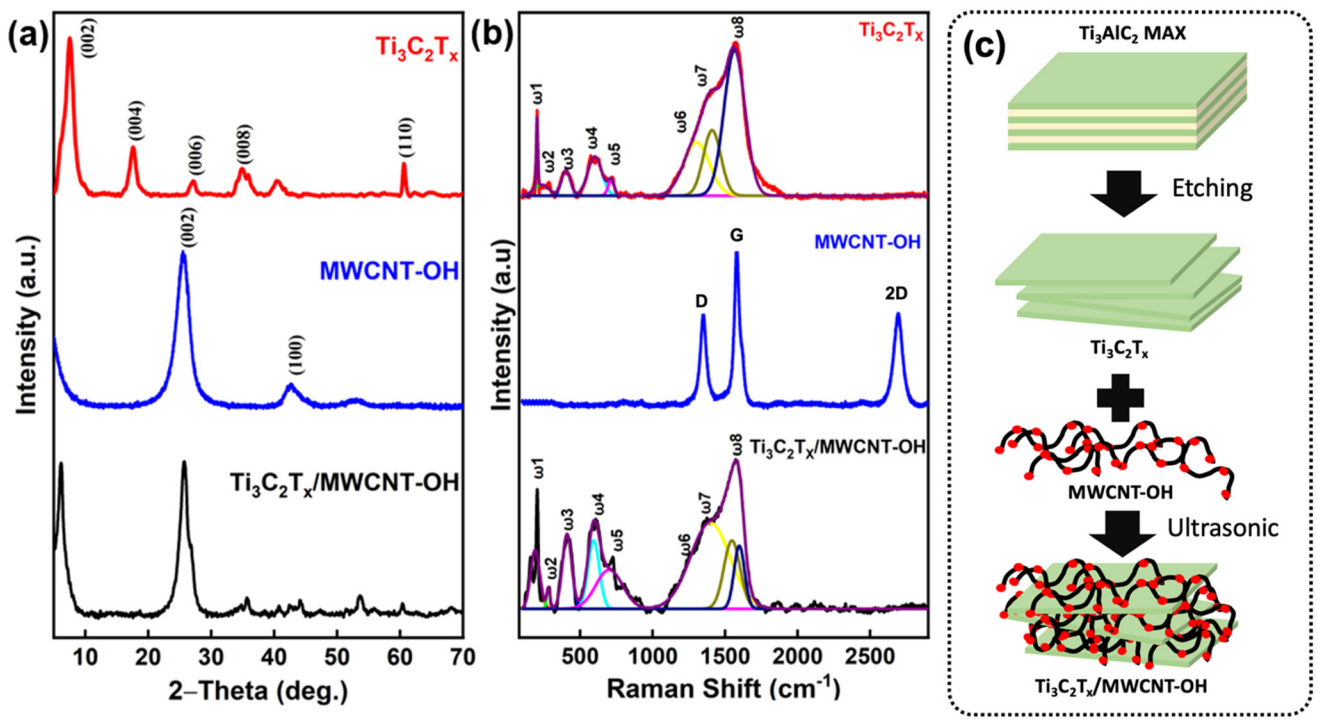

Fig. 1 (a) X-ray diffractogram and (b) Raman spectra of $Ti_3C_2T_x$, MWCNT-OH, and $Ti_3C_2T_x$/MWCNT-OH nanocomposites; (c) schematic illustration for the formation of nanocomposite.

The Raman spectrum of the as-prepared $Ti_3C_2T_x$ exhibited the characteristics of Raman shift corresponding to the A_{1g} (ω1 and ω3), E_g (ω2, ω3, and ω4), D (ω6 and ω7), and G (ω8) bands. This is primarily due to the fact that $Ti_3C_2T_x$ belongs to the D_{3d} group which is represented as $4E_g + 2A_{1g} + 4E_u + 2A_{2u}$, where E_g and A_{1g} are Raman-active modes, while E_u and A_{2u} are IR-active modes.[44–46] The Raman spectrum of MWCNT-OH showed three distinct peaks at 1340 cm^{-1} (D band), 1582 cm^{-1} (G band), and 2690 cm^{-1} (2D band). The estimated intensity ratio of the D to G bands was also found to be considerably high (0.8), indicating the successful functionalization of MWCNT. Furthermore, the Raman spectra of the nanocomposite exhibited the appearance of characteristic peaks of both $Ti_3C_2T_x$ and MWCNT-OH, which suggests the successful integration of the two materials during the ultrasonic irradiation process. Fig. 1c presents the schematic illustration for the assembly of $Ti_3C_2T_x$ and MWCNT-OH to make the $Ti_3C_2T_x$/MWCNT-OH composite.

XPS was also carried out to determine the surface chemistry of the as-prepared $Ti_3C_2T_x$. As shown in Fig. 2a, the high-resolution spectra of C 1s exhibited three major peaks which can be further deconvoluted into five centered peaks at 289.2, 287.0, 284.9, and 281.7 eV, which correspond to COO, CH_x/CO, C–C, C–Ti, respectively.[47–49] The appearance of C–O was most likely due to the side oxidation of $Ti_3C_2T_x$ form TiO_2 and carbon atom network within its structure.[47] Further analysis on Ti 2p high-resolution spectra revealed that the deconvoluted spectrum consisted of eight major peaks, indicating the various oxidation states of the Ti atom (Fig. 2b). The spectrum was fitted with a fixed ratio of 2 : 1 for the two doublets of Ti $2p_{3/2}$ and Ti $2p_{1/2}$, each comprising four components. Based on the results, the peaks of Ti $2p_{1/2}$ for Ti–O, Ti^{3+}, Ti^{2+}, and Ti–C were observed at binding energies of 465.2, 463.8, 461.4, and 460.3 eV, respectively. The binding energies of Ti $2p_{3/2}$ for Ti–O, Ti^{3+}, Ti^{2+}, and Ti–C were observed at 459.5, 457.2, 456.2, and 455.2 eV, respectively. These peak assignments were in

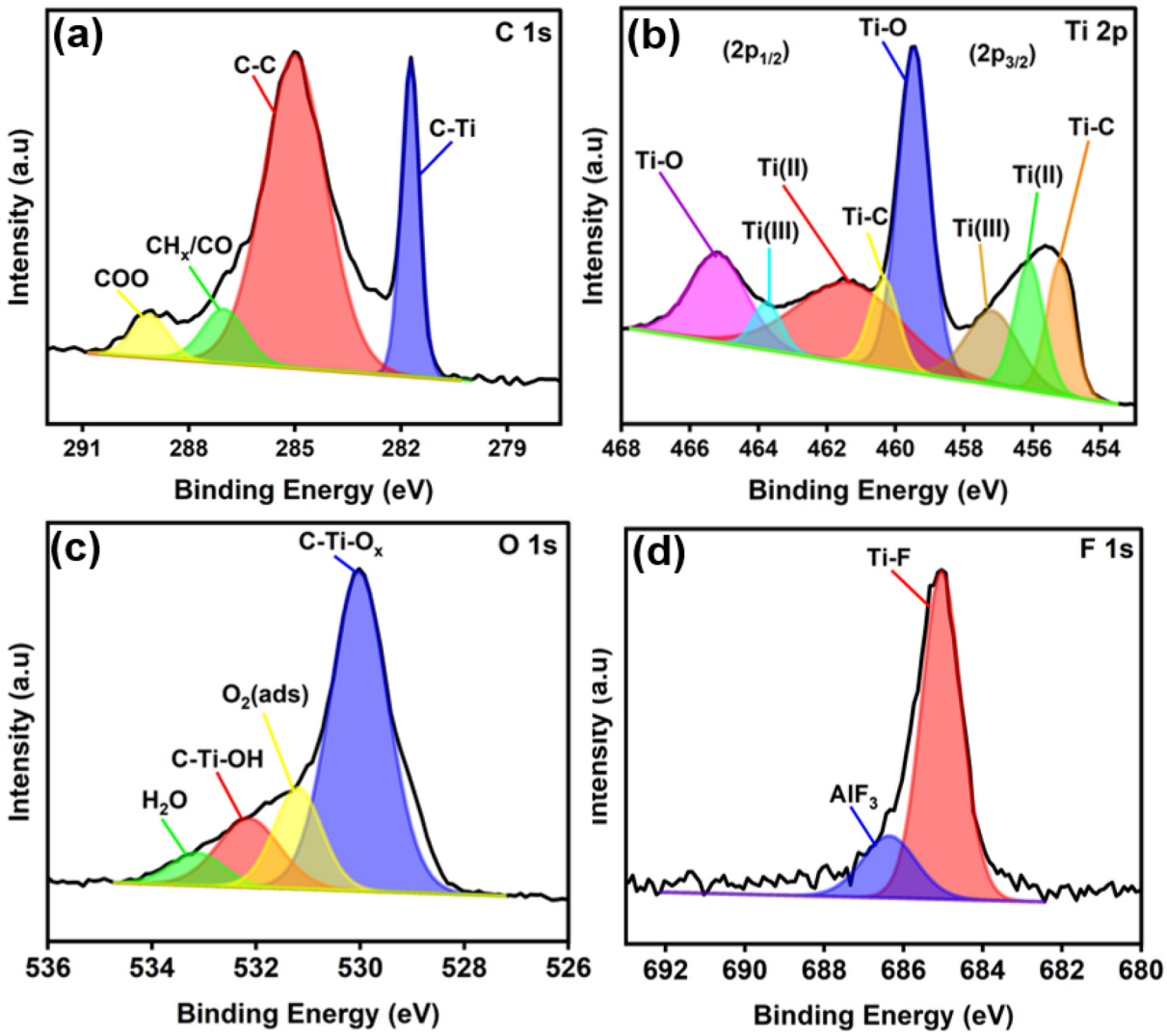

Fig. 2 High resolution XPS spectra of (a) C 1s, (b) Ti 2p, (c) O 1s, and (d) F 1s of the as-prepared $Ti_3C_2T_x$.

good agreement with previous studies elsewhere.[48,50,51] The O 1s spectrum could also deconvoluted into four peaks at 530.1, 532.2, 531.2, and 533.2 eV, which were attributed to the surface species of C–Ti–O_x, C–Ti–OH, adsorbed oxygen and water, respectively (Fig. 2c). Interestingly, F 1s sore spectrum revealed the presence of a mixture of –F, –OH, and –O termination groups on the as-prepared $Ti_3C_2T_x$, as evidenced by the appearance of strong Ti–F peak at 685.0 eV (Fig. 2d).

Fig. 3 shows micrographic images of the samples obtained from HRTEM and FESEM. The results indicate that the as-prepared $Ti_3C_2T_x$ exhibits the anticipated sheet-like morphology, which originates from the etching and exfoliation process of Ti_3AlC_2 (Fig. 3a and b). The formation of $Ti_3C_2T_x$ is further supported by the SAED pattern, confirming the hexagonal structure of MXene. Furthermore, FESEM images further confirmed the successful functionalization of MWCNT, displaying a rougher surface morphology and increased intermolecular interactions, evidencing the presence of OH groups and indicating successful surface modification (Fig. 3c). In addition, the result also demonstrated that the as-prepared MWCNT-OH exhibited a well-preserved multiwalled structure with minimal defects, indicating controlled functionalization. As shown in Fig. 3d (inset), SAED analysis showed the characteristic diffraction patterns of the hexagonal lattice structure of graphitic carbon with ring patterns corresponding to (002), (006), and (101) planes, confirming the crystalline nature of MWCNT. Furthermore, the as-prepared nanocomposite exhibited a well-integrated hybrid structure, where $Ti_3C_2T_x$ nanosheets were found to be uniformly distributed and intimately interfaced with MWCNT-OH (Fig. 3e and f). The MWCNT-OH strands were observed to be wrapping around and bridging in between sheets of $Ti_3C_2T_x$, indicating a strong interaction between the materials. This suggests that the integration using ultrasonic irradiation was able to produce a homogeneous composite morphology which ultimately enhanced the overall surface roughness.

Electrochemical behavior

In this study, the electrochemical behavior of paraoxon was initially evaluated using cyclic voltammetry with a bare GCE. As shown in Fig. 4a, it is evident that there were no observable reduction nor oxidation peaks in the blank electrolyte (0.1 M phosphate buffer at pH 7) at a scan rate of 50 mV s^{-1}. However, when 1 mM of paraoxon-ethyl was added to the electrolyte a sharp cathodic peak appeared at −0.67 V *vs.* Ag/AgCl. This is believed to be due to the reduction of paraoxon-ethyl (A) into phenylhydroxylamine (B), involving a transfer of four electrons and four protons (system I, Fig. 4d).[52,53] Interestingly, two additional peaks indicating a reversible redox reaction were observed at −0.13 V (cathodic) and −0.12 V

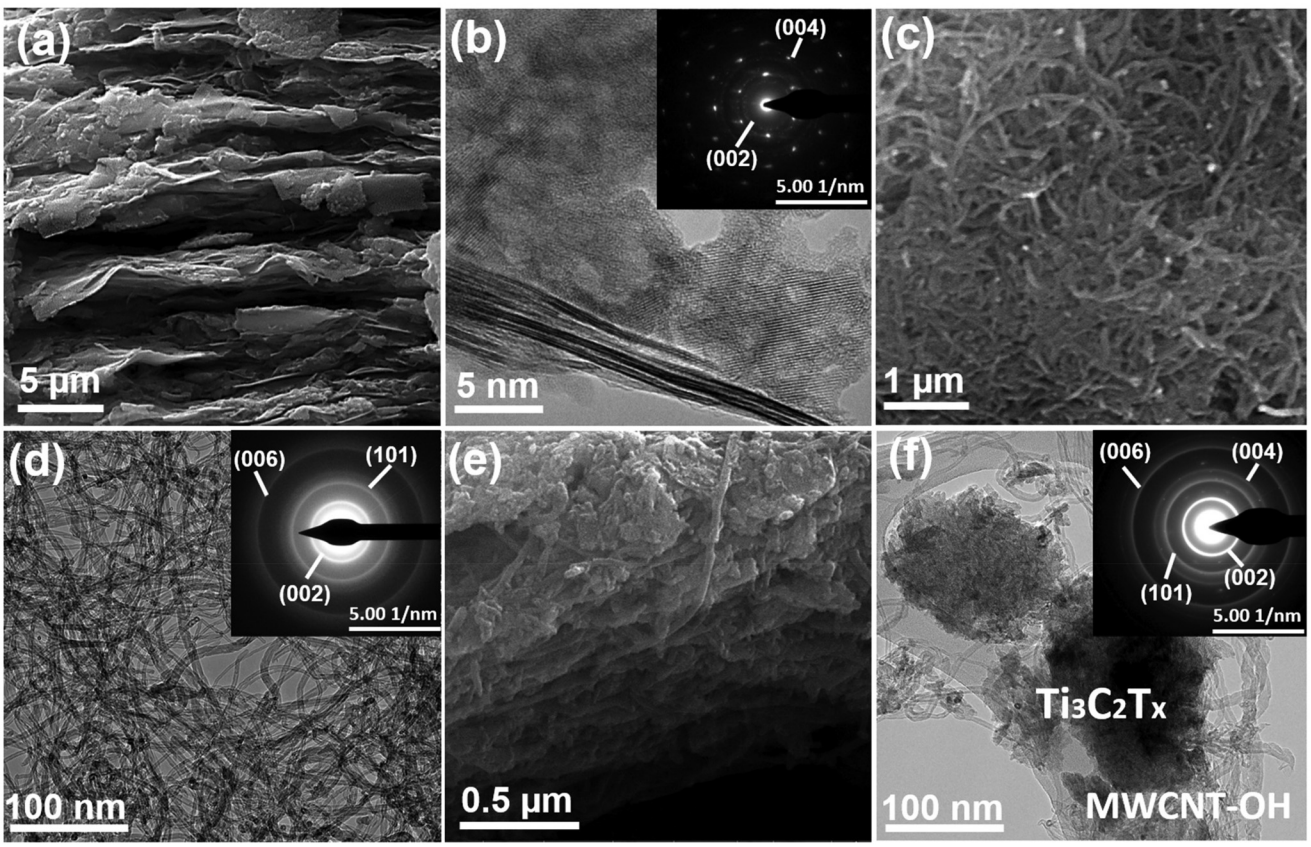

Fig. 3 FESEM and HRTEM images (insets: SAED analysis) of (a and b) $Ti_3C_2T_x$, (c and d) MWCNT-OH, and (e and f) $Ti_3C_2T_x$/MWCNT-OH nanocomposite, respectively.

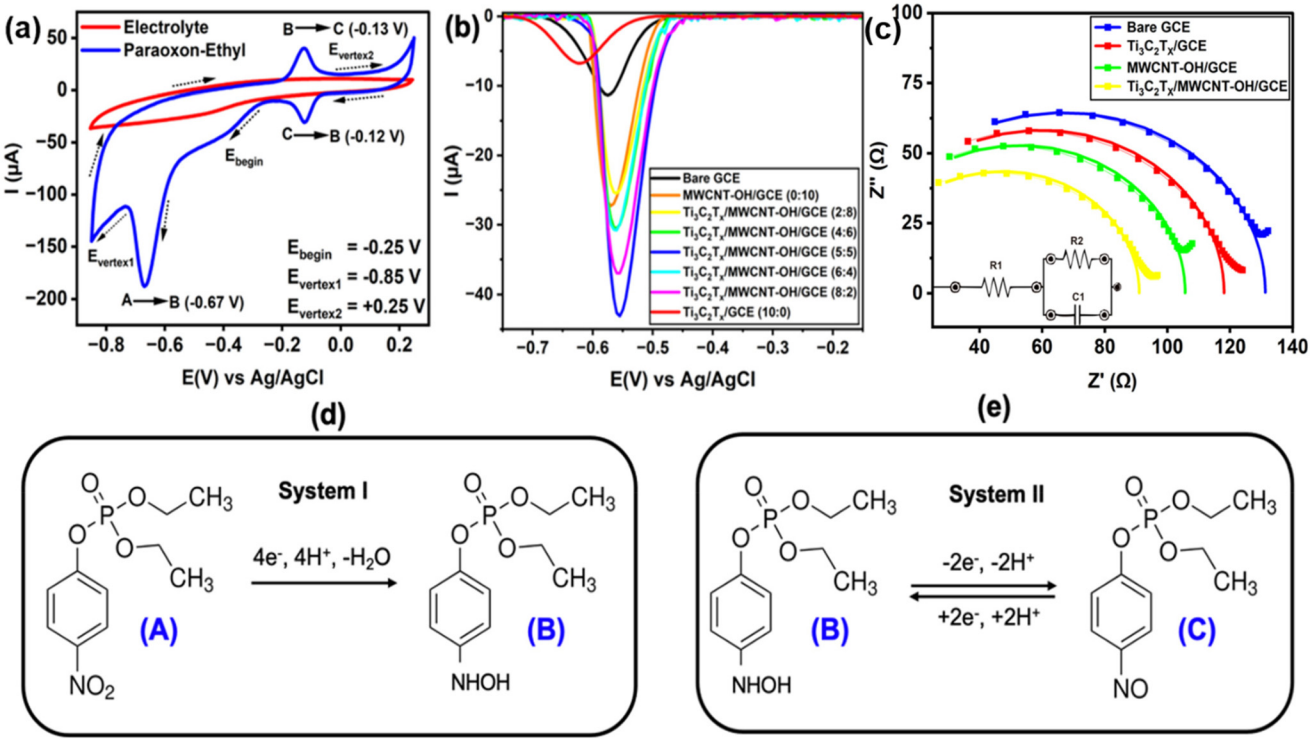

Fig. 4 (a) Cyclic voltammogram of 100 μM paraoxon-ethyl in 0.1 M phosphate buffer solution (PBS) at pH 7.0 using bare GCE; (b) differential pulse voltammogram of paraoxon-ethyl measured using different types of electrodes; (c) Nyquist plot of different type of electrodes using 5 mM $K_3[Fe(CN)_6]$; and the proposed electrochemical redox reaction of paraoxon-ethyl according to (d) system I and (e) system II.

(anodic) *vs.* Ag/AgCl. The occurrence of these pair of peaks was primarily due to the reversible transformation of the hydroxylamine group in phenylhydroxylamine (B) into nitroso group (C), involving the exchange of two electrons and two protons (system II, Fig. 4e).[52,53] However, it is worth noting that the current of the two peaks responsible for redox reactions in system II was significantly smaller than that of system I. Therefore, we decided to utilize the first electrochemical reduction of paraoxon-ethyl according to system I as the potential basis for further investigations.

A series of electrochemical investigations utilizing DPV was further conducted to examine the effect of various sensing electrode materials. Fig. 4b shows the differential pulse voltammogram of 0.1 mM paraoxon-ethyl in a 0.1 M phosphate buffer at pH 8, measured using various types of sensing electrodes composed of $Ti_3C_2T_x$, MWCNT-OH, and their composite at different ratios. The results clearly indicate that the nanocomposite exhibited significantly higher current responses compared to the individual $Ti_3C_2T_x$ or MWCNT-OH. Interestingly, the highest current was obtained with the $Ti_3C_2T_x$/MWCNT-OH nanocomposite at a 5 : 5, which is attributed to the synergistic effect between $Ti_3C_2T_x$ and MWCNT-OH which facilitates a more efficient reduction of paraoxon-ethyl into phenylhydroxylamine. This enhancement is believed to stem from the improved electrical conductivity resulting from the combination of these two materials, which facilitates efficient electron transport.[54] Additionally, functionalization of MWCNT with OH groups plays a crucial role in ensuring uniform interaction with $Ti_3C_2T_x$, thereby increasing the density of active sites and enhancing catalytic activity.[55,56] The uniform distribution of the composite also prevents aggregation and hence maximizing the exposure of catalytic sites. Moreover, the available surface functional groups on the nanocomposite contribute to the adsorption of paraoxon-ethyl onto the catalyst surface *via* various interactions, including hydrogen bonding, van der Waals force, π–π interactions, and electrostatic attractions, ultimately enhancing the overall catalytic efficiency.[35,57–60]

Furthermore, EIS studies were also performed of −0.68 V *vs.* Ag/AgCl to evaluate electron transfer properties at the electrode/electrolyte interface. Fig. 4c presents Nyquist plots for the three-electrode types: bare GCE, $Ti_3C_2T_x$/GCE, and $Ti_3C_2T_x$/MWCNT-OH/GCE (ratio: 5 : 5). The result demonstrates that the nanocomposite electrode showed a smaller semi-circular diameter compared to the individual materials, indicating higher conductivity and lower resistivity. This trend further demonstrated that the combination of $Ti_3C_2T_x$ and MWCNT-OH yields a synergistic effect that significantly improves the electrical properties of the composite. The enhanced conductivity and reduced resistivity were primarily attributed to the efficient electron transfer pathways facilitated by the well-distributed and uniform integration of $Ti_3C_2T_x$ nanosheets with MWCNT-OH. The high electric conductivity of $Ti_3C_2T_x$ along with the extensive conductive network

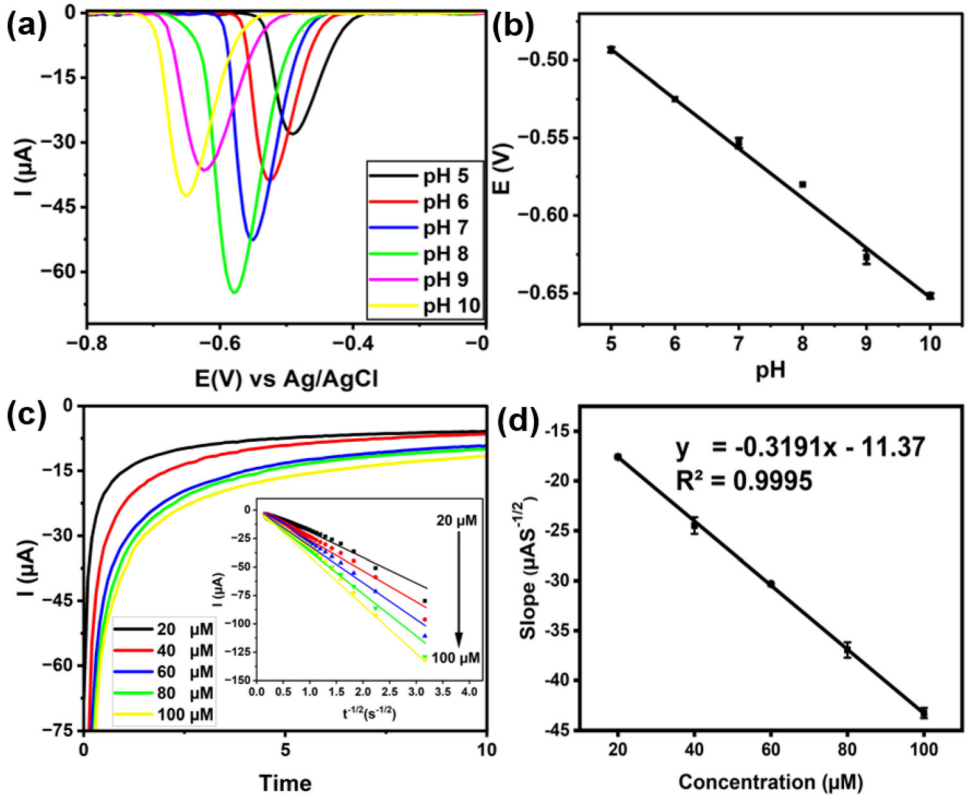

Fig. 5 Effect of (a) pH and (b) scan rate on the detection of 0.1 mM of paraoxon-ethyl; (c) chronoamperogram of paraoxon-ethyl at various concentrations (insets: Cottrell plot) and (d) the corresponding plot of Cottrell slope *vs.* paraoxon-ethyl concentration.

provided by MWCNT-OH affords multiple routes for electron flow, thereby minimizing charge transfer resistance.[61,62] This improved electron transfer capability was crucial for the reduction of paraoxon-ethyl. The combination of high surface area, abundant active sites, and enhanced conductivity results in a higher current output and overall superior electrocatalytic performance of the nanocomposite. This is corroborated by the estimation of resistance values of charge transfer (R_2) using the Randles circuit analysis. Typically, a higher R_2 value reflects slower electron transfer processes at the electrolyte/electrode interface. The measured R_2 values for GCE, $Ti_3C_2T_x$/GCE, MWCNT-OH/GCE, and $Ti_3C_2T_x$/MWCNT-OH/GCE were found to be 129.1, 116.5, 106.8 Ω, and 87.1 Ω, respectively.

Optimization of sensing conditions

To optimize sensing conditions of the as-prepared nanocomposite electrode for the detection of paraoxon-ethyl, a series of DPV measurements were initially performed in 0.1 M phosphate buffer at various pH conditions. As shown in Fig. 5a, the reduction for paraoxon-ethyl was observed to shift toward a higher potential as the pH increased. Interestingly, the potential was found to be linearly correlated with pH (see Fig. S2, ESI†). This suggests that the reduction of paraoxon-ethyl is thermodynamically less preferable in a basic medium. This phenomenon can be attributed to the involvement of four protons in the reduction of paraoxon-ethyl according to system I (Fig. 4d), making the reaction more favorable in acidic conditions.[63,64] Nevertheless, it is noteworthy that the highest current was obtained when the measurement was conducted at pH 8, despite the reduction occurring at a moderate potential (−0.68 V *vs.* Ag/AgCl). At low pH, the nanocomposite is most likely to begin disintegrating due to the acidic environment, which could degrade the functional groups and weaken the interaction between $Ti_3C_2T_x$ and MWCNT-OH. Such disintegration and degradation could further reduce the number of active sites and disrupt the conductive network within the composite, leading to decreased catalytic efficiency and lower current output. Therefore, despite the higher reduction potential at increased pH, the optimal DPV measurement was achieved at pH 8 which balances the stability of the nanocomposite and the catalytic activity. The improved reaction kinetics and the prevention of nanocomposite disintegration at higher pH levels outweigh the disadvantage of the increased reduction potential, resulting in the observed optimum performance.

Furthermore, the effect of scan rate on the detection of paraoxon-ethyl was also investigated by varying the scan rate from 25 to 150 mV s^{-1} (Fig. 5b). The result showed that higher scan rates result in higher current, which can be attributed to the increased rate of electron transfer at the electrode surface. This phenomenon is observed because higher scan rates

reduce the time available for diffusion of the electroactive species to the electrode surface, thereby increasing the reliance on the electron transfer kinetics. Additionally, the slight shift of the cathodic peak towards negative values with increasing scan rate was also found to be linearly correlated with the logarithm of the scan rate. This trend suggests an increase in the overpotential required for the reduction reaction (see Fig. S3, ESI†). This shift aligns with the expected behavior for irreversible electrochemical reactions, as described by Laviron's theory.[65] In this case, the calculated electron transfer coefficient (α) was found to be 0.44, which indicates a symmetrical energy barrier for electron transfer. According to the theory, a reaction with α value close to 0.5 is most likely to have electron transfer as the rate-determining step rather than the diffusion of reactants.

In addition, chronoamperometry was also performed at various concentrations of paraoxon-ethyl to determine its diffusion coefficient on the surface of electrode using the Cottrell equation, which can be expressed as follows:

$$I(t) = \frac{nFAD^{1/2}C}{\pi^{1/2}t^{1/2}} \quad (2)$$

where n represents the total number of electrons involved in the reaction, D indicates the diffusion coefficient ($cm^2\ s^{-1}$), F is Faraday's constant, A is the electrode area (0.31 cm^2, which was obtained *via* cyclic voltammetry, see Fig. S4, ESI†), and C represents the concentration (mol cm^{-3}).

Fig. 5c presents the chronoamperogram of paraoxon-ethyl at various concentrations and the corresponding fitting to the Cottrell equation. Meanwhile, Fig. 5d shows the corresponding correlation between Cottrell slopes *vs.* concentration. Based on the result, the diffusion coefficient was found to be approximately 3.19×10^{-9} $cm^2\ s^{-1}$ (eqn (S1)†). This value provides crucial information about the rate at which paraoxon-ethyl molecules diffuse through the solution to reach the electrode surface, which is a key factor in the overall efficiency of the electrochemical detection process. This diffusion coefficient value is considered moderately high for small organic molecules in aqueous solutions. In comparison to other similar molecules, it is believed that paraoxon-ethyl diffuses relatively quickly, enabling it to reach the electrode surface efficiently.[66] This rapid diffusion is beneficial for electrochemical sensing applications as it ensures that the analyte is readily available at the electrode surface for reduction, leading to a more pronounced and faster current response.[67] Furthermore, this moderately high diffusion coefficient also indicates that the nanocomposite was well-suited for detecting paraoxon-ethyl over a range of concentrations, as it can handle the flux of incoming molecules without significant delays.

Sensing performances

Fig. 6a shows the performance of the nanocomposite electrode in paraoxon-ethyl detection using the DPV technique. The results demonstrate that the nanocomposite exhibited excellent sensing performance over a broad concentration range from 1 to 100 μM. A linear increase in peak current with increasing paraoxon-ethyl concentration was observed, indicating a strong correlation between the analyte concentration and the electrochemical response of the nanocomposite electrode. This linear relationship between the peak current (I_{pc}) and concentration, as depicted in the calibration plot (Fig. 6a inset), highlights the efficient interaction between paraoxon-ethyl molecules and the active sites on the nanocomposite surface. The nanocomposite's performance is attributed to its specific mechanism, where the adsorption of analyte molecules onto its surface facilitates efficient electron transfer, enhancing the electrochemical response and ensuring high sensitivity across the tested concentration range.

Moreover, the overall LOD and LOQ showed that the nanocomposite maintained high sensitivity towards paraoxon-ethyl detection. Based on the estimation from S/N ratio, the values of LOD and LOQ for the nanocomposite were found to be 0.01 and 0.07 μM, respectively. The combination of a high diffusion coefficient and the superior catalytic property of the nanocomposite ensures rapid and effective reduction of paraoxon-ethyl molecules, resulting in a strong and reliable current response. Moreover, the performance of the as-prepared electrode was also found to be comparable with other materials reported elsewhere (Table 1).

Furthermore, the detection of paraoxon-ethyl using the nanocomposite electrode was also evaluated in the presence of various potential interfering substances, including diazinon, carbaryl, Fe^{2+}, NO_2^-, NO_3^-, ascorbic acid, and glucose. As shown in Fig. 6b, these potential interferents exhibited negligible or minimal effect on the detection of paraoxon-ethyl, with recovery values of exceeding 95%. This robustness can be attributed to the selective catalytic properties of the nanocomposite, which effectively differentiates paraoxon-ethyl from other substances. The specific functional groups and high surface area of the nanocomposite provide numerous active sites that favor the adsorption and reduction of paraoxon-ethyl while minimizing non-specific interactions with other molecules. Besides, it is postulated that the electrochemical properties of nanocomposite allow for a distinct potential window where the reduction of paraoxon-ethyl occurs, reducing the likelihood of overlapping signals from interfering species. The strong electron transfer capability and high conductivity of the nanocomposite further ensure that the signal corresponding to paraoxon-ethyl remains clear and unimpeded by the presence of other substances. Consequently, the nanocomposite electrode demonstrates excellent selectivity and reliability in detecting paraoxon-ethyl, even in complex matrices with various potential interferences.

The reproducibility and stability of the electrode for paraoxon-ethyl detection were evaluated to demonstrate its reliability and robustness. Fig. 6c and d present the results obtained from both reproducibility and stability tests, respectively. Here, reproducibility was assessed by measuring the current response across six different electrodes, yielding a RSD of 4.2%. This low RSD value indicates minimal variation in the

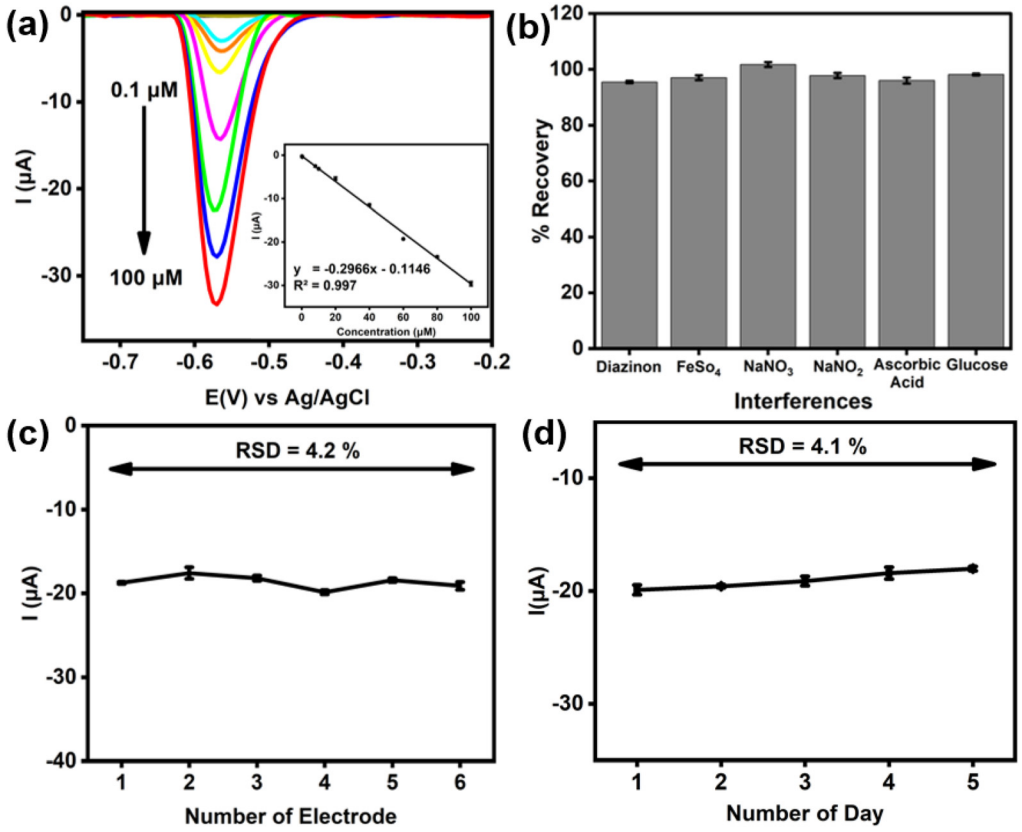

Fig. 6 (a) Performance of the nanocomposite in paraoxon-ethyl detection using DPV technique (inset: calibration plots), (b) variation in reduction current of paraoxon-ethyl measurements in the presence of several interfering species when measured with $Ti_3C_2T_x$/MWCNT-OH (N = 3), (c) reproducibility using six different electrodes (N = 3), (d) stability over 5 consecutive days of paraoxon-ethyl measurements at a concentration of 80 μM in 0.1 M phosphate buffer pH 8 (N = 3).

Table 1 Comparison of sensing performance of the as-prepared nanocomposite with various sensors reported elsewhere

Electrode material	Linear range (μM)	LOD (nM)	Sensitivity (μA μM^{-1} cm^{-2})	Ref.
$Ti_3C_2T_x$/MWCNT-OH	0.1–100	10	0.957	This work
$BiOV_4$	0.2–1.96	30	0.345	68
Au–Ag core–shell/graphene/PEDOT:PSS	0.2–100	10	3.24	53
Zn–Ni–P–S/GO	1–200	35	0.064	69
CuNSs@BSASWCNT	0.05–35	12.8	n/a	66
MWCNT/SiC/AgNP	0.0055–0.549	20.9	0.018	70
CS-c-MWCNT-HA	5–80	100	0.00510	67

current responses, highlighting the consistency and uniformity in the fabrication of the nanocomposite electrodes. The uniform distribution of $Ti_3C_2T_x$ and MWCNT-OH in the nanocomposite likely contributes to the high reproducibility, ensuring that each electrode has a similar density of active sites and conductive pathways. The stability was evaluated by testing the same electrode over a five-day period, resulting in an RSD of 4.1%. This result demonstrates that the electrode was able to maintain good performance over time without significant degradation. The stability of the nanocomposite can be attributed to the strong interactions between $Ti_3C_2T_x$ and MWCNT-OH, which prevent the detachment or degradation of the active materials. Additionally, the robust structural integrity of the nanocomposite ensures that the active sites remain accessible and functional over prolonged periods of use.

Finally, the practical application of the as-prepared electrode for the measurement of real fruit samples (red and green grapes) spiked with paraoxon-ethyl was evaluated using the standard addition method. As shown in Fig. 7, the results showed a highly linear relationship between current and concentration, with R^2 values of 0.9996 at a concentration of 9.146 ± 0.37 μM for green grapes and 0.9991 at 12.57 ± 0.40 μM for red grapes, respectively. These high correlation coefficients indicate excellent sensitivity and accuracy. Additionally, the recovery values for paraoxon-ethyl detection at each concentration exceeded 97%, validating the electrode's effectiveness and reliability. This high recovery rate ensures accurate quantification of the spiked paraoxon-ethyl without significant interference from the fruit matrices. As expected, the specific functional groups and high surface area of the nanocomposite

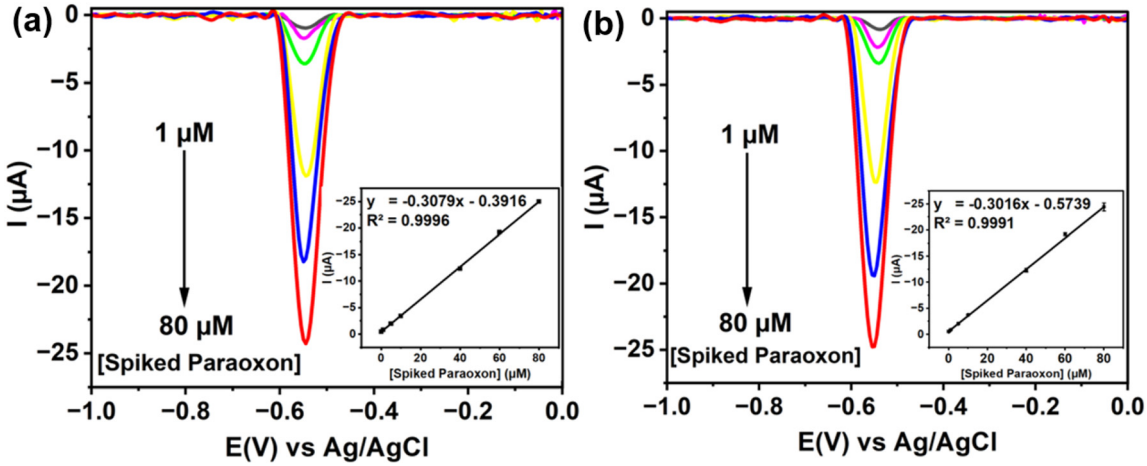

Fig. 7 Voltammograms at a scan rate of 50 mV s^{-1} using $Ti_3C_2T_x$/MWCNT-OH from measurements in pH 8 phosphate buffer at various concentrations of paraoxon-ethyl ranging from 1 to 80 μM in samples (a) green grapes and (b) red grapes.

provide numerous active sites for selective adsorption and reduction of paraoxon-ethyl. The strong electron transfer capability and high conductivity further enhance detection performance, ensuring clear signals even in complex samples.

Conclusions

In summary, as-prepared electrodes fabricated from $Ti_3C_2T_x$/MWCNT-OH nanocomposite demonstrated excellent performance for non-enzymatic electrochemical detection of paraoxon-ethyl. The comprehensive material characterizations confirmed the structural integrity, high conductivity, and low resistivity of the nanocomposite, contributing to its superior catalytic properties. Additionally, DPV analysis revealed the sensor's exceptional performance, exhibiting a highly linear response over a broad concentration range. The calibration plots demonstrated distinct characteristics, indicative of high sensitivity and low detection thresholds. Operating at pH 8, the sensor demonstrated a linear detection range spanning from 0.1 to 100 μM, with a detection limit of 10 nM and high sensitivity values of 0.9568 μA μM^{-1} cm^{-2}. The electrode's performance was further distinguished by its remarkable selectivity, reproducibility, and stability. It maintained consistent results across multiple uses and over extended periods. The practical applicability of the electrode was validated through tests on real fruit samples (red and green grapes), which yielded high recovery rates and showed minimal interference from other substances present in the complex matrices. These findings highlight the potential of the $Ti_3C_2T_x$/MWCNT-OH nanocomposite as a practical, reliable, and sustainable tool for environmental monitoring and food safety applications, particularly in detecting trace levels of paraoxon-ethyl. This advancement not only aligns with current regulatory demands but also represents a significant step forward in the development of sensitive and reliable sensors for monitoring environmental and food contaminants, setting a benchmark for future innovations in nanocomposite-based electrochemical sensors.

Data availability

The data that support the findings of this study are available from the corresponding author upon reasonable request.

Conflicts of interest

There are no conflicts to declare.

Acknowledgements

M.K. and F.A.A.N. greatly appreciate the financial support provided by the Indonesian Endowment Fund for Education (LPDP) on behalf of the Indonesia Ministry of Education, Culture, Research and Technology and managed by Universitas Indonesia under INSPIRASI Program (grant no. PRJ-61/LPDP/2022 and 612/E1/KS.06.02/2022). This work is also supported by the Singapore National Research Foundation (NRF Investigatorship NRF-NRFI09-0002), and the Directorate General of Higher Education, Research, and Technology, The Ministry of Education, Culture, Research, and Technology, Republic of Indonesia, under the Penelitian Fundamental Reguler research funding scheme (contract no. 027/E5/PG.02.00.PL/2024 and 22101/IT3.D10/PT.01.03/P/B/2024). A.H. acknowledges the support from the Indonesia Endowment Funds for Education (LPDP) and National Research and Innovation Agency under Riset dan Inovasi untuk Indonesia Maju (RIIM) scheme (grant no. 82/II.7/HK/2022).

References

1 M. Z. Abedeen, M. Sharma, H. S. Kushwaha and R. Gupta, *TrAC, Trends Anal. Chem.*, 2024, **176**, 117729.
2 L. Ding, J. Guo, S. Chen and Y. Wang, *Talanta*, 2024, 125937.
3 V. Rajagopalan, S. Venkataraman, D. S. Rajendran, V. V. Kumar, V. V. Kumar and G. Rangasamy, *Environ. Res.*, 2023, 115724.
4 M. Akilarasan, E. Tamilalagan and S.-M. Chen, *J. Environ. Chem. Eng.*, 2024, **12**, 111928.
5 J. Kaushal, M. Khatri and S. K. Arya, *Ecotoxicol. Environ. Saf.*, 2021, **207**, 111483.
6 H. Mali, C. Shah, B. Raghunandan, A. S. Prajapati, D. H. Patel, U. Trivedi and R. Subramanian, *J. Environ. Sci.*, 2023, **127**, 234–250.
7 M. Gao, Z. Ni, G. Li, G. Wu and B. Huang, *Int. J. Mol. Sci.*, 2023, **24**, 14213.
8 G. Horn, T. Demel, S. Rothmiller, N. Amend and F. Worek, *Clin. Toxicol.*, 2024, 1–8.
9 S. Khazaie, M. Jafari, M. Golamloo, A. Asgari, J. Heydari, M. Salehi and F. Salem, *Biochemistry*, 2023, **88**, 165–178.
10 S. Ayaz, S. Uluçay, A. Üzer, Y. Dilgin and R. Apak, *Talanta*, 2024, **266**, 124962.
11 R. E. Baynes and J. M. Bowen, *J. AOAC Int.*, 1995, **78**, 812–814.
12 N. Kamelipour, A. Mohsenifar, M. Tabatabaei, T. Rahmani-Cherati, K. Khoshnevisan, A. Allameh, M. M. Milani, S. Najavand and B. Etemadikia, *Microchim. Acta*, 2014, **181**, 239–248.
13 B. Li, P. Sun, J. Zhen, W. Gong, Z. Zhang, W. Jia, G. Liang and L. Pan, *Sens. Actuators, B*, 2021, **348**, 130715.
14 J. Turan, M. Kesik, S. Soylemez, S. Goker, S. Coskun, H. E. Unalan and L. Toppare, *Sens. Actuators, B*, 2016, **228**, 278–286.
15 K. Wang, L. Wang, W. Jiang and J. Hu, *Talanta*, 2011, **84**, 400–405.
16 Y. Shastak and W. Pelletier, *J. Appl. Anim. Res.*, 2024, **52**, 2321957.
17 M. Wan, Y.-s. Li, Y.-X. Luo, H. Li and X.-F. Gao, *Anal. Biochem.*, 2023, **664**, 115045.
18 B. R. Putra, U. Nisa, R. Heryanto, M. Khalil, F. Khoerunnisa, A. Ridhova, Y. N. Thaha, F. Marken and W. T. Wahyuni, *Analyst*, 2022, **147**, 5334–5346.
19 B. R. Putra, U. Nisa, R. Heryanto, E. Rohaeti, M. Khalil, A. Izzataddini and W. T. Wahyuni, *Anal. Sci.*, 2022, **38**, 157–166.
20 E. Saepudin, T. Yuliani, M. A. F. Nasution, M. Khalil, J. W. Hong and T. A. Ivandini, *Makara J. Sci.*, 2021, **25**, 1.
21 W. T. Wahyuni, B. R. Putra, H. A. Rahman, T. A. Ivandini, Irkham, M. Khalil and I. Rahmawati, *ACS Omega*, 2023, **9**, 1497–1515.
22 H. K. Kordasht and M. Hasanzadeh, *J. Mol. Recognit.*, 2020, **33**, e2832.
23 T. Mahmudiono, D. O. Bokov, S. A. Jasim, W. K. Abdelbasset and D. M. Khashirbaeva, *Microchem. J.*, 2022, **179**, 107460.
24 M. A. Khan, F. Ramzan, M. Ali, M. Zubair, M. Q. Mehmood and Y. Massoud, *Nanomaterials*, 2023, **13**, 780.
25 A. K. Mia, M. Meyyappan and P. Giri, *Biosensors*, 2023, **13**, 169.
26 K. Xie, J. Wang, S. Xu, W. Hao, L. Zhao, L. Huang and Z. Wei, *Mater. Des.*, 2023, **228**, 111867.
27 R. Wu, J. Hao and Y. Wang, *Small*, 2024, **20**, 2404821.
28 S. Ganesan, K. Ramajayam, T. Kokulnathan and A. Palaniappan, *Molecules*, 2023, **28**, 4617.
29 A. G. Juandito, D. S. Khaerudini, S. Priyono, G. T. Kadja, D. Djuhana and M. Khalil, *J. Nanopart. Res.*, 2024, **26**, 110.
30 M. Khalil, M. Lesa, A. G. Juandito, A. R. Sanjaya, T. A. Ivandini, G. T. Kadja, M. H. Mahyuddin, M. Sookhakian and Y. Alias, *Mater. Adv.*, 2023, **4**, 3853–3862.
31 U. Pratomo, R. A. Pratama, A. P. Sulaeman, G. T. Kadja, M. Khalil and I. Primadona, *Mater. Lett.*, 2023, **337**, 133932.
32 L. Yu, J. Chang, X. Zhuang, H. Li, T. Hou and F. Li, *Anal. Chem.*, 2022, **94**, 3669–3676.
33 F. Zhao, Y. Yao, C. Jiang, Y. Shao, D. Barceló, Y. Ying and J. Ping, *J. Hazard. Mater.*, 2020, **384**, 121358.
34 A. Appu Mini and V. Raghavan, *Microchem. J.*, 2024, **201**, 110674.
35 Z. Fu, Q. Chen, J. He, S. Li, R. Ming, Y. Wei, Y. Xu, J. Liu and L. Zhang, *Compos. Sci. Technol.*, 2023, **242**, 110155.
36 E. Mari, M. Duraisamy, M. Eswaran, S. Sellappan, K. Won, P. Chandra, P.-C. Tsai, P.-C. Huang, Y.-H. Chen and Y.-C. Lin, *Microchim. Acta*, 2024, **191**, 212.
37 H. Xing, X. Li, Y. Lu, Y. Wu, Y. He, Q. Chen, Q. Liu and R. P. Han, *Sens. Actuators, B*, 2022, **361**, 131704.
38 M. Dong, O. Tomes, A. Soul, Y. Hu, E. Bilotti, H. Zhang and D. G. Papageorgiou, *ACS Appl. Nano Mater.*, 2024, **7**, 3314–3325.
39 L. Tian, M. Jiang, M. Su, X. Cao, Q. Jiang, Q. Liu and C. Yu, *Microchem. J.*, 2023, **185**, 108172.
40 M. Alhabeb, K. Maleski, B. Anasori, P. Lelyukh, L. Clark, S. Sin and Y. Gogotsi, *Chem. Mater.*, 2017, **29**, 7633–7644.
41 G. T. Kadja, S. A. Natalya, F. Balqis, N. J. Azhari, N. Nurdini, A. Sumboja, R. S. Rahayu, U. Pratomo and M. Khalil, *Nano-Struct. Nano-Objects*, 2023, **36**, 101059.
42 X.-F. Luo, C.-H. Yang, Y.-Y. Peng, N.-W. Pu, M.-D. Ger, C.-T. Hsieh and J.-K. Chang, *J. Mater. Chem. A*, 2015, **3**, 10320–10326.
43 D. K. Singh, P. K. Iyer and P. K. Giri, *Diamond Relat. Mater.*, 2010, **19**, 1281–1288.
44 T. O. Colak, C. T. Altaf, F. N. T. Yesilbag, Y. O. Yesilbag, I. D. Yildirim, E. Erdem, F. B. Misirlioglu, N. D. Sankir and M. Sankir, *J. Energy Storage*, 2024, **86**, 111274.
45 T. Hu, J. Wang, H. Zhang, Z. Li, M. Hu and X. Wang, *Phys. Chem. Chem. Phys.*, 2015, **17**, 9997–10003.
46 A. Sarycheva and Y. Gogotsi, *Chem. Mater.*, 2020, **32**, 3480–3488.

47 Y. Cao, Q. Deng, Z. Liu, D. Shen, T. Wang, Q. Huang, S. Du, N. Jiang, C.-T. Lin and J. Yu, *RSC Adv.*, 2017, **7**, 20494–20501.
48 W. Y. Chen, X. Jiang, S.-N. Lai, D. Peroulis and L. Stanciu, *Nat. Commun.*, 2020, **11**, 1302.
49 S. Shah, T. Habib, H. Gao, P. Gao, W. Sun, M. Green and M. Radovic, *Chem. Commun.*, 2017, **53**, 400–403.
50 Y. T. Liu, P. Zhang, N. Sun, B. Anasori, Q. Z. Zhu, H. Liu, Y. Gogotsi and B. Xu, *Adv. Mater.*, 2018, **30**, 1707334.
51 R. B. Rakhi, B. Ahmed, M. N. Hedhili, D. H. Anjum and H. N. Alshareef, *Chem. Mater.*, 2015, **27**, 5314–5323.
52 G. Liu and Y. Lin, *Electrochem. Commun.*, 2005, **7**, 339–343.
53 W. T. Wahyuni, B. R. Putra, H. A. Rahman, W. Anindya, J. Hardi, E. Rustami and S. N. Ahmad, *ACS Omega*, 2024, **9**, 2896–2910.
54 B. Freitas, W. G. Nunes, D. M. Soares, F. C. Rufino, C. M. Moreira, L. M. Da Silva and H. Zanin, *Mater. Adv.*, 2021, **2**, 4264–4276.
55 M. Aakyiir, J.-A. Oh, S. Araby, Q. Zheng, M. Naeem, J. Ma, P. Adu, L. Zhang and Y.-W. Mai, *Compos. Sci. Technol.*, 2021, **214**, 108997.
56 S. Gholami, J. L. Llacuna, V. Vatanpour, A. Dehqan, S. Paziresh and J. L. Cortina, *Chemosphere*, 2022, **294**, 133699.
57 Ü. Çakır, F. Kestel, B. K. Kızılduman, Z. Bicil and M. Doğan, *Diamond Relat. Mater.*, 2021, **120**, 108604.
58 Y. Cheng, Y. Xie, H. Cao, L. Li, Z. Liu, S. Yan, Y. Ma, W. Liu, Y. Yue and J. Wang, *Chem. Eng. J.*, 2023, **453**, 139823.
59 S. Lim, J. H. Kim, H. Park, C. Kwak, J. Yang, J. Kim, S. Y. Ryu and J. Lee, *RSC Adv.*, 2021, **11**, 6201–6211.
60 E. M. Pérez and N. Martín, *Chem. Soc. Rev.*, 2015, **44**, 6425–6433.
61 M. P. Bilibana, *Adv. Sens. Energy Mater.*, 2023, 100080.
62 S. Zhang, B. Cheng, Z. Gao, D. Lan, Z. Zhao, F. Wei, Q. Zhu, X. Lu and G. Wu, *J. Alloys Compd.*, 2022, **893**, 162343.
63 E. Aamer, J. Thöming, M. Baune, N. Reimer, R. Dringen, M. Romero and I. Bösing, *Sci. Rep.*, 2022, **12**, 16380.
64 V. A. Okello, I. O. K'Owino, K. Masika and V. O. Shikuku, *Sustainability*, 2022, **14**, 9451.
65 R. Nehru and S.-M. Chen, *Nanoscale Adv.*, 2020, **2**, 3033–3049.
66 H. Bagheri, A. Afkhami, H. Khoshsafar, A. Hajian and A. Shahriyari, *Biosens. Bioelectron.*, 2017, **89**, 829–836.
67 M. Stoytcheva, R. Zlatev, G. Montero, Z. Velkova and V. Gochev, *Biotechnol. Biotechnol. Equip.*, 2018, **32**, 213–220.
68 P. K. Gopi, D. B. Ngo, S.-M. Chen, C. H. Ravikumar and W. Surareungchai, *Chemosphere*, 2022, **288**, 132511.
69 B. Xiao, *Int. J. Electrochem. Sci.*, 2022, **17**, 220672.
70 I. Chuasontia, W. Sirisom, N. Nakpathomkun, S. Toommee, C. Pechyen, B. Tangnorawich and Y. Parcharoen, *Micromachines*, 2023, **14**, 1613.